ELSEVIER

Polymer 44 (2003) 3037–3043

polymer

www.elsevier.com/locate/polymer

Quantitative phase contrast imaging of arborescent graft polystyrene by off-axis transmission electron holography

Tseng-Ming Chou[a,1], Matthew Libera[a,*], Mario Gauthier[b]

[a]*Department of Chemical, Biochemical, and Materials Engineering, Stevens Institute of Technology, Hoboken, NJ 07030, USA*
[b]*Department of Chemistry, Institute for Polymer Research, University of Waterloo, Waterloo, Ont., Canada N2L 3G1*

Received 11 October 2002; received in revised form 3 February 2003; accepted 5 February 2003

Abstract

Imaging nanoscale polymer objects in the Transmission Electron Microscope is difficult, because small polymeric objects interact only weakly with intermediate-energy electrons. Heavy element staining can induce significant amplitude contrast, but stains can introduce artifacts that complicate the structure determination at nanometer length scales. This paper explores transmission electron holography for phase contrast imaging of unstained arborescent graft polystyrene nanoparticles. Holography is able to recover significant phase contrast from these particles despite the fact that there is negligible amplitude contrast. Comparative imaging experiments show that off-axis holography provides substantially higher contrast than that generated by the traditional method of transferring phase information to amplitude information via defocus. This effect is a consequence of different lens contrast-transfer behavior in each of these two imaging approaches. Under kinematical conditions when the appropriate mean inner potential is known, the specimen's projected thickness can be directly mapped from the holographic phase image to give a measure of the specimen's three-dimensional shape. Such quantitative imaging shows that individual arborescent graft polystyrene nanoparticles, which are spherical in a good solvent, adopt a flattened shape when deposited on a carbon substrate and allowed to dry.

Keywords: Quantitative phase contrast; Polystyrene; Transmission electron holography

1. Introduction

Globular macromolecular structures such as dendrimers, hyperbranched polymers, and micro/nanoemulsions have been increasingly studied over the past decade [1–5]. These all possess unique thermodynamic and rheological properties due to their small size which can range from a few nanometers to hundreds of nanometers. Their size and flexible chemical functionality make them very suitable for drug delivery in pharmaceutical applications, and their self-assembling properties make them of increasing interest to a variety of patterning technologies.

Real-space characterization of such polymeric nanostructures can be achieved using the high resolution of the transmission electron microscope (TEM). Generally speaking, amorphous polymeric materials do not scatter electrons strongly and, therefore, they typically do not provide high contrast using bright-field TEM imaging. Most amorphous polymers, as well as many semicrystalline polymers, thus require staining prior to examination in the TEM. Staining preferentially labels chemically active sites with heavy elements such as osmium, ruthenium, or uranium, among other possibilities. These high atomic number (Z) elements increase the high-angle Rutherford scattering and provide a source of strong amplitude contrast between stained and unstained specimen features. Staining approaches have made and will continue to make significant contributions to the general understanding of multiphase polymeric materials at low and medium resolution. However, staining can lead to artifacts that interfere with image interpretation at fine length scales. Artifacts such as the accumulation of staining nanocrystals (e.g. oxides and salts) around nanoparticles supported on a carbon grid [6], or the enhanced contrast typically observed at surfaces and interphase boundaries, often can not be avoided by creative specimen preparation. Instead, alternate imaging methods must be explored which generate contrast based on the

* Corresponding author. Tel.: +1-201-2165259; fax: +1-201-2168306.
E-mail address: mlibera@stevens-tech.edu (M. Libera).
[1] Present address: Emispec Systems, Inc., Tempe, AZ 85282, USA.

0032-3861/03/$ - see front matter © 2003 Elsevier Science Ltd. All rights reserved.
doi:10.1016/S0032-3861(03)00159-9

intrinsic interaction between the incident electrons and the unstained specimen. Phase contrast imaging is one such alternative.

Modulation of the electron wave phase by unstained polymers can be significant despite the fact that the amplitude modulation is weak. In the absence of magnetic or electric fields and strong Bragg interference, the phase shift, $\Delta\phi(x,y)$, is due to the electron refraction caused by the mean inner potential, Φ_0. Under kinematical conditions, it can be described as [7]:

$$\Delta\phi(x,y) = C_E \Phi_0 t(x,y) \tag{1}$$

C_E is an energy-dependent constant given as:

$$C_E = \frac{\lambda E}{2\pi}\frac{2E_0 + E}{E_0 + E} \tag{2}$$

where E and λ are the electron energy and wavelength, respectively, and E_0 is the electron rest energy. The mean inner potential (Φ_0) is very sensitive to the distribution of valence electrons [8–10] and is thus expected to lead to differential phase shifts when an electron wave passes through a multiphase polymer.

Phase contrast imaging of unstained multiphase polymers based on defocus methods to exploit mean inner potential differences has been studied in a series of papers by Thomas et al. [11–13]. The transfer properties of the microscope convert phase information into amplitude information, and the amplitude information can subsequently be recovered from the recorded image intensity. Again, however, because the electron scattering strength of most polymers is so much weaker than that of most metals, ceramics, and semiconductors, significant defocus must be applied to generate contrast from polymeric specimens. The same is true of most biological specimens. Defocus introduces interference fringes near surfaces and interfaces that in turn complicate image interpretation.

Phase contrast imaging by transmission electron holography provides an alternate means of recovering phase modulations from weakly scattering systems such as organic polymers and biological structures [14–18]. Despite the fact that holographic approaches have been known for many decades [19,20], widespread application of the method was limited until the development and commercialization of robust field-emission electron sources with sufficient coherence to render holographic interference experiments practical [21,22]. We have used electron holography to collect phase images from nanospherical particles of polystyrene, PS, as well as of silicon [23,24]. The spherical geometry enables one to determine the specimen thickness at any given point in the specimen and, using Eq. (1), to subsequently remove the thickness contribution to the electron wave phase shift. The remaining contribution can be directly related to the mean inner potential. This previous work determined that the PS mean inner potential is 8.4 V.

In the present paper we describe work which relaxes the spherical-specimen constraint. Here we study arborescent graft polystyrene nanoparticles [25–28]. These are globular macromolecular structures with controllable dimensions. While they are spherical when solvated, deposition on a substrate together with solvent removal can compress their shape. We use these as model specimens to show that holography can recover substantial phase contrast near focus despite the fact that there is negligible amplitude contrast. Using the previously determined value of Φ_0^{PS}, we then recover the projected thickness from the phase image. The contrast generated by holographic imaging at focus is then compared to that generated during a through-focus series using the more traditional phase contrast transfer properties of the microscope and shows that the holographic approach gives substantially higher contrast than the defocus method.

2. Relevant imaging theory

This section briefly outlines the mathematical framework underlying imaging first by defocus [29] and then by holography [30]. It comes from well-established literature. For simplicity, we assume that the specimen behaves as a so-called weak phase object such that modulation of the wave amplitude by the specimen does not occur and any phase modulation is small. Given that we are studying specimens tens of nanometers or less in thickness and composed of light elements, this is a reasonable approximation. For a weak phase object, the exit-face wavefunction, $\psi(\underline{r})$, can be approximated as:

$$\psi(\underline{r}) = A(\underline{r})e^{-i\phi(\underline{r})} \sim 1 - i\sigma\Phi(\underline{r}) \tag{3}$$

where $\sigma = \pi/\lambda E$ is the interaction constant and $\Phi(\underline{r})$ is the projected electrostatic potential of the specimen. The parameter σ can be recovered from Eq. (2) when $E_0 \gg E$. When the exit-face wave is acted upon by the objective lens, it is modulated by the lens transfer function $t(\underline{r}) = c(\underline{r}) + is(\underline{r})$. In a real-space representation, the exit-face wavefunction is convoluted with the lens transfer function. Assuming unit magnification, the intensity recorded is given by:

$$\begin{aligned} I(\underline{r}) &= |[1 - i\sigma\Phi(\underline{r})] * (\underline{r})|^2 \\ &= |[1 - i\sigma\Phi(\underline{r})] * [c(\underline{r}) + is(\underline{r})]|^2 \end{aligned} \tag{4}$$

or

$$I(\underline{r}) \sim 1 + 2\sigma\Phi(\underline{r}) * s(\underline{r}) \tag{5}$$

The lens transfer function is given as:

$$t(\underline{r}) = F[T(\underline{q})] = F[B(\underline{q})e^{i\chi(\underline{q})}] \tag{6}$$

where F represents a Fourier transform, $B(\underline{q})$ is an aperture function, and $\underline{q}$ is a reciprocal-space vector which measures spatial frequencies. The effects of defocus, Δf, and spherical aberration, C_s, are accounted for by the phase factor in

Eq. (6):

$$\chi(\underline{q}) = \pi\lambda\Delta f q^2 + \frac{1}{2}\pi C_s \lambda^3 q^4 \tag{7}$$

$c(\underline{r})$ and $s(\underline{r})$ correspond to the Fourier transforms of the real and imaginary parts of $T(\underline{q})$, respectively:

$$c(\underline{r}) = F[B(\underline{q})\cos\chi(\underline{q})] \text{ and } s(\underline{q}) = F[B(\underline{q})\sin\chi(\underline{q})] \tag{8}$$

$\sin\chi(\underline{q})$ is commonly referred to as the *phase contrast transfer function*, because it transfers modulation of the wave phase into a modulation of amplitude. In a traditional imaging experiment, amplitude information can be recovered when the wave intensity is recorded by a camera (Eq. (5)). Without transfer, no phase information would be recovered. Since $\chi(\underline{q})$ is a function of defocus, the nature and extent of this transfer can, to some extent, be controlled. Contrast in an image recorded by defocus in a bright-field mode is given by:

$$C = \frac{I(\underline{r}) - I_{min}}{I_{max} + I_{min}} \tag{9}$$

where I_{min} and I_{max} are the minimum and maximum intensities within a particular image.

A holographic imaging experiment is designed to recover both the wave amplitude and the wave phase [31,32]. After passing through the specimen, the exit-face wave function, modulated by the lens transfer, is combined with an unmodulated reference wave. With sufficient coherence between them, these two waves interfere. The recorded intensity is then given by:

$$I_{holo}(\underline{r}) = |\psi(\underline{r}) * t(\underline{r}) + \psi_{ref}(\underline{r})|^2 \tag{10}$$

where $\psi(\underline{r})$ is the specimen-modulated, exit-face wavefunction and $\psi_{ref}(\underline{r})$ is the unmodulated reference wave function. Expression (10) can be evaluated to give:

$$\begin{aligned} I_{holo}(\underline{r}) &= 1 + |\psi(\underline{r}) * t(\underline{r})|^2 \\ &+ 2|\psi(\underline{r}) * t(\underline{r})|\cos[2\pi q_c \cdot \underline{r} + \Delta\phi(\underline{r})] \end{aligned} \tag{11}$$

The final term in this expression describes a set of cosinusoidal fringes at a given carrier frequency, q_c, with phase shifts, $\Delta\phi(\underline{r})$, and amplitude, $A(\underline{r}) = 2|\psi(r) * t(r)|$ that represent, respectively, the phase and amplitude of the image wave.

Reconstruction of the hologram first involves the application of a Fourier transform to the intensity distribution of Eq. (11). The result is:

$$\begin{aligned} F\{I_{holo}(r)\} &= \delta(\underline{q}) + \Psi(\underline{q})T(\underline{q}) * \Psi^*(\underline{q})T^*(\underline{q}) \\ &+ \delta(\underline{q} + \underline{q_c}) * \psi(\underline{q})T(\underline{q}) \\ &+ \delta(\underline{q} - \underline{q_c}) * \psi^*(\underline{q})T^*(\underline{q}) \end{aligned} \tag{12}$$

The first term is a delta function. The second is the autocorrelation function, which in the case of a weak phase object is identical to the expression given by Eq. (4). The third and fourth terms correspond to sidebands offset in reciprocal space from the autocorrelation function by the carrier frequency, q_c, of the holographic interference fringes.

The reconstruction procedure continues by isolation of one of the two sidebands using a numerical aperture followed by an inverse transform to recover the holographic image wave function, $\psi_{holo}(\underline{r})$:

$$\psi_{holo}(\underline{r}) = F^{-1}\{\Psi(\underline{q})T(\underline{q})\} = \psi(\underline{r}) * t(r) \tag{13}$$

For a weak phase object, the reconstructed holographic wavefunction is given as:

$$\begin{aligned} \psi_{holo}(\underline{r}) &= [1 - i\sigma\Phi(\underline{r})] * c(\underline{r}) + is(\underline{r})] \\ &= 1 + \sigma\Phi(\underline{r}) * s(\underline{r}) - i[\sigma\Phi(\underline{r}) * c(\underline{r})] \end{aligned} \tag{14}$$

The wave amplitude is given by $|\psi_{holo}(\underline{r})|$, and the wave phase is given by:

$$\begin{aligned} \tan[\Delta\phi(\underline{r})] &= \frac{-\sigma\Phi(\underline{r}) * c(\underline{r})}{1 - \sigma\Phi(\underline{r}) * s(\underline{r})} \\ \Rightarrow \Delta\phi(\underline{r}) &\sim \frac{-\sigma\Phi(\underline{r}) * c(\underline{r})}{1 - \sigma\Phi(\underline{r}) * s(\underline{r})} \end{aligned} \tag{15}$$

where we have invoked the small angle approximation. In the context of a phase image that maps the spatial dependence of $\Delta\phi$ in two dimensions, the relevant measure of contrast is:

$$C = \frac{\Delta\phi(\underline{r}) - \Delta\phi_{min}}{\Delta\phi_{max} + \Delta\phi_{min}} \tag{16}$$

We will see in Section 4 that the contrast associated with a holographic phase image is substantially higher than that of a phase image generated by defocus. We attribute this to the fact that for a significant range of spatial frequencies, particularly those that carry information at length scales of order 1 nm and higher, the term $\sigma\Phi(\underline{r}) * s(\underline{r})$ is close to zero while the term $\sigma\Phi(\underline{r}) * c(\underline{r})$ is finite and relatively constant.

3. Experimental procedure

Arborescent graft polymers (AGPs) based on polystyrene were used as specimens throughout this work. The particular specimens studied were designated G3-5k indicating that they are third generation structures synthesized from 5k molecular weight polystyrene precursors. These were synthesized following methods described in the literature [25,26]. Neutron scattering shows that the present G3-5k PS AGP has a spherical shape in solution with an average diameter of 53 nm [33]. Atomic force microscopy (AFM) indicates that the particles tend to flatten when cast onto a mica substrate [34]. For the studies reported here, AGP solutions were diluted in toluene to a concentration of approximately 0.1 wt%. A drop of this solution was placed on a Cu TEM grid with a supportive carbon film. After

solvent evaporation, the specimens could immediately be examined in the TEM with no further preparation.

The electron microscopy was performed at Stevens using a Philips CM 20 FEG TEM/STEM at an accelerating voltage of 200 kV. The manufacturer's specification for its spherical aberration coefficient, C_s, is 2.0 mm. This instrument has a high brightness, high coherence Schottky field emission gun (FEG) electron source. Its selected area aperture (SA) mechanism has been modified [35] to incorporate a Mollenstedt electrostatic biprism [36] which is central to the off-axis electron holography technique [22, 31]. Both holograms and focal-series images were recorded digitally using a 1k × 1k Gatan 794 Multiscan camera. This camera affords sufficient recording linearity and dynamic range for efficient holographic imaging experiments. Holograms were reconstructed using the HoloWorks package within Gatan's Digital Micrograph software package.

4. Results and discussion

Fig. 1 shows a low magnification bright-field image of AGP PS nanoparticles on a carbon substrate. This specimen was stained by exposure to RuO_4 vapor at room temperature for one hour. The average diameter of projected AGP particles observed in images such as these is ~50 nm. This is smaller than the neutron-scattering data for these same particles in solution, presumably because of solvent swelling effects that are absent in the TEM experiments. Images such as that in Fig. 1 say little concerning the three dimensional shape of an individual particle. Furthermore, this image displays two common artifacts associated with staining. First, there is an accumulation of stain at the surface as can be seen by the rim of dark contrast around the edge of the particle. This rim would be absent if the stain was uniformly distributed throughout the entire particle. Second, RuO_2 nanoparticles deposit on the particle surface as well as on the surrounding carbon substrate. Because of their random orientation, they lead to speckled contrast that increases image noise and degrades resolution. These RuO_2 nanocrystals are evident in the high-resolution image inset to Fig. 1. While different staining protocols such as shorter exposure to the RuO_4 vapor change the details of these staining effects, the artifactual structure remains.

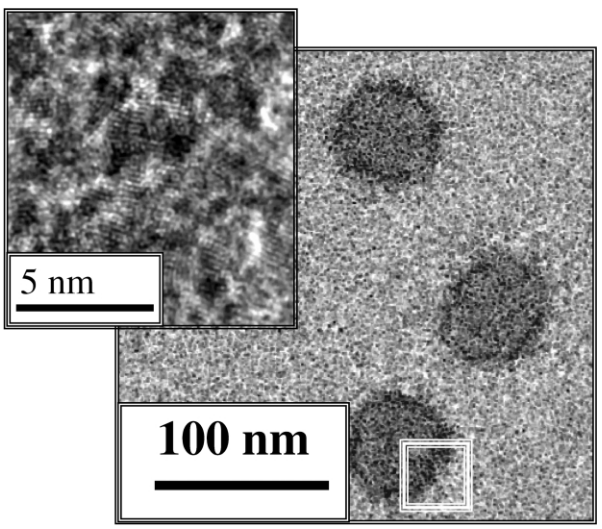

Fig. 1. Bright-field TEM image of RuO_4-stained arborescent graft polystyrene particles on a thin carbon film. The inset is a high-resolution image showing RuO_2 oxide nanoparticles on the sample surface.

Unstained versions of these same specimens were studied by phase contrast imaging. Fig. 2 shows a typical result of holographic imaging. Fig. 2a shows the raw hologram. The inset enlarges a small portion of the hologram to better show the cosinusoidal interference fringes. Digital reconstruction of the hologram begins by taking a Fast Fourier Transform (FFT) of the hologram together with an empty reference hologram. The result is shown in Fig. 2b. The FFT has a central autocorrelation function together with two sidebands. A digital aperture isolates one sideband that is subsequently back transformed to recover the complex exit-face wavefunction. For the purposes of the holographic imaging experiments reported here, the transfer properties of the objective lens were assumed to be constant over the relevant range of frequencies.

Phase and amplitude images, where $\Delta\phi(x, y)$ and $A(x, y)$

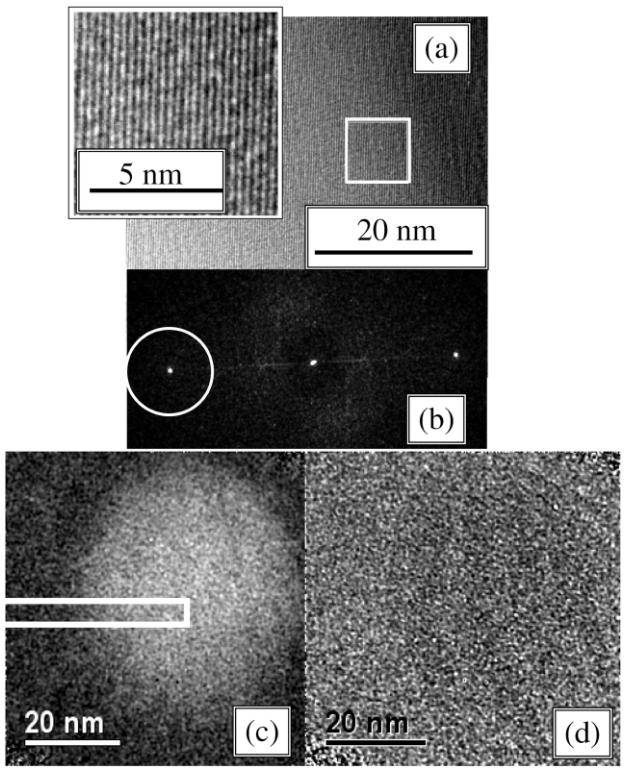

Fig. 2. (a) Electron hologram of an arborescent graft polystyrene particle. The enlarged inset shows the holographic interference fringes; (b) FFT of the hologram shows the autocorrelation and two sidebands; (c) reconstructed phase image; and (d) reconstructed amplitude image.

are mapped, are shown in Fig. 2c and d, respectively. The phase image displays significant contrast representing the AGP PS particle on the carbon support film despite the fact that the amplitude image shows essentially none. This basic result is independent of the size of the digital aperture used to isolate the sideband and reconstruct the exit-face wavefunction. It was also reproduced in several different holographic imaging experiments using different specimens. This is a significant result. It experimentally confirms the hypothesis that, at focus, the weak-phase object properties of such a nanoscale polymer specimen can give rise to recoverable phase information in the absence of any significant amplitude modulation of the electron wave by the specimen.

Given an experimental dataset describing $\Delta\phi(x, y)$ and knowing the mean inner potential characteristic of polystyrene from previous work [24], phase data such as that in Fig. 2c can be converted into a measure of the projected specimen thickness using Eq. (1). Fig. 3 shows this conversion for the subset of phase data described by averaging the 20-pixels-wide rectangular selection in Fig. 2c running from the particle center to beyond its edge. Fig. 3a shows the profile of phase shift data, and Fig. 3b shows the result of the conversion to a thickness profile. The solid line in Fig. 3b represents a second-order polynomial fit to these thickness data. Since the reference wave in these experiments sampled the carbon substrate rather than vacuum, no measure of substrate thickness could be made. Hence, the average background signal was set to zero.

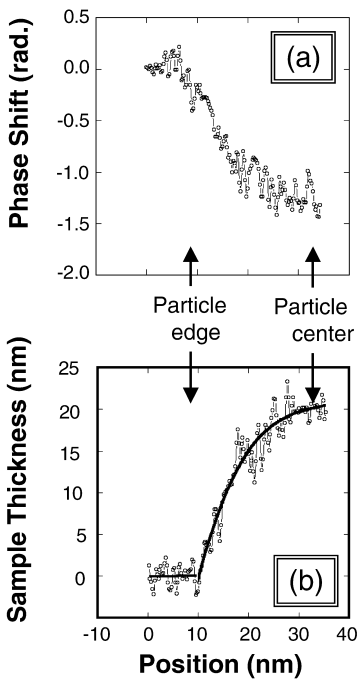

Fig. 3. (a) Phase shift retrieved from Fig. 2(c) as a function of position from the particle edge to its center; (b) thickness profile of the AGP particle with a second order polynomial fit (solid line).

Fig. 3 shows that the maximum particle height is approximately 23 nm. Its diameter, however, is approximately 51 nm. This quantitative imaging shows that the AGP PS particle is not spherical, as might be concluded based on the traditional stained image (Fig. 1). Instead, the particle has a pancake shape. This shape presumably forms during solvent evaporation when the solvated particle wets the carbon substrate and is kinetically frozen in that configuration once sufficient solvent has evaporated to render the particle rigid. This result is similar to the findings of previous AFM work [34] but is less ambiguous since edge distortion effects due to the finite tip dimensions are avoided.

Combining phase-shift and thickness data from Fig. 3, one can develop a measure of contrast as a function of particle thickness. The result is given in Fig. 4. The conversion of holographic data uses the definition given in Eq. (16) together with the calibration between thickness and radial position given by the polynomial fit in Fig. 3b. The contrast generated by the holographic phase image increases significantly as specimen thickness increases.

Fig. 4 also shows an experimentally derived relation between contrast and thickness for phase contrast imaging experiments based on defocus. The data are derived from the results of through-focal series imaging of the same unstained specimens used in the holographic imaging. Salient results from one such through-focal series are given in Fig. 5. The focal step for this particular series was $\Delta f = 48$ nm with 33 different images collected. $\Delta f = 0$ corresponds to the minimum-contrast condition. The image data were normalized to unity by dividing every pixel value in an image by the average background intensity characteristic of that same image. The intensity profiles from each image show that the intensity deviation relative to background varies with defocus. The noise associated with these profiles clearly increases with defocus for the defoci

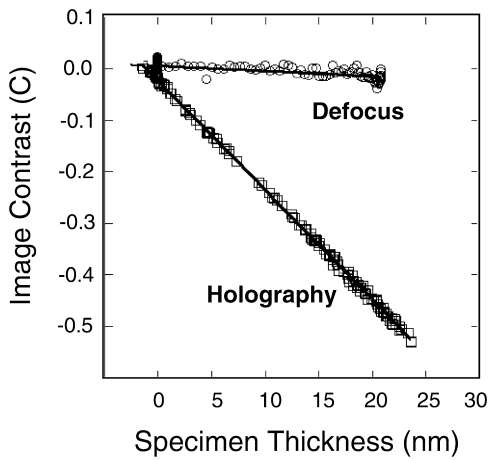

Fig. 4. Image contrast versus sample thickness for AGP particles imaged by defocus phase contrast imaging (●) at focus ($\Delta f = 0$) and holographic phase contrast imaging (□)at focus ($\Delta f = 0$).

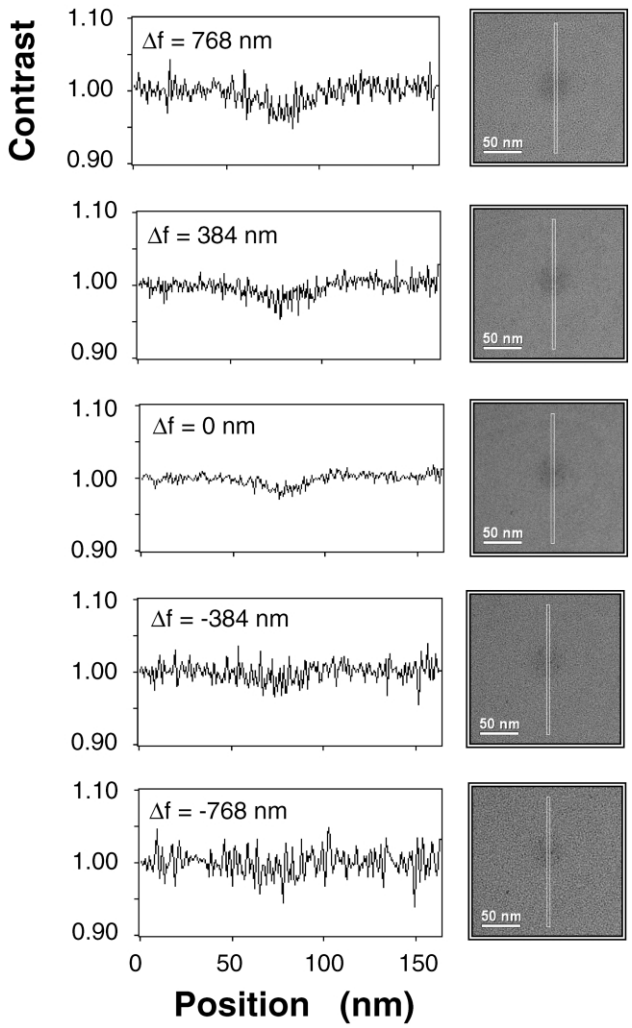

Fig. 5. Focal series images and intensity profiles across an AGP PS particle.

addressed here. These findings are representative of the images of the focal series not included in Fig. 5. The contrast-thickness relation given in Fig. 4 representing the defocus experiment is derived from the intensity profile data given in Fig. 5 together with the definition given by Eq. (9) and the thickness/radial position relation given by the polynomial fit (Fig. 3b).

Fig. 4 shows that the contrast derived from the phase contrast image at zero defocus is substantially less than that provided by holographic phase imaging at zero defocus. The phase contrast generated by increasing the defocus does not significantly affect this finding. Furthermore, increasing defocus comes at the expense of an increase in image noise. At extremely large defocus values of order microns, in excess of those presented here, the defocus degrades resolution and complicates the image contrast by sign changes in the transfer when passing different spatial frequencies.

The difference in contrast generated by the holographic and defocus approaches can be understood by

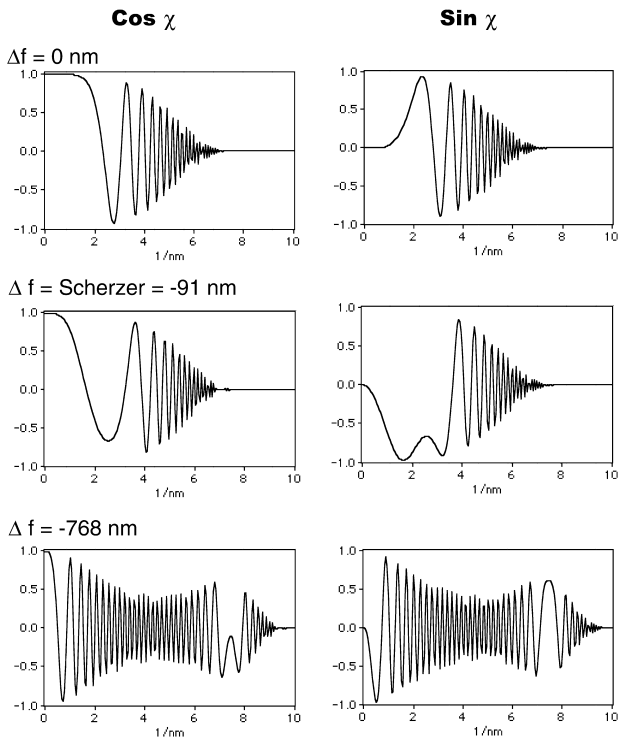

Fig. 6. The cosine and sine terms of the microscope transfer function for different values of microscope defocus.

considering the amplitude and phase transfer properties of the microscope. As given by Eqs. (6)–(8), the microscope lens transfer function consists of cosine and sine terms that each depend on defocus and spherical aberration. Fig. 6 shows the $\cos\chi$ and $\sin\chi$ terms calculated for focus values of 0, −91 (Scherzer defocus), and −768 nm. Consider first the curves for $\Delta f = 0$. The $\cos\chi$ term is equal to unity for spatial frequencies approaching 2 nm. Over this same range of spatial frequencies, the $\sin\chi$ term is essentially zero. For higher frequencies, both terms oscillate in a manner that complicates image interpretation. As the defocus increases, the passband where $\cos\chi \sim 1$ and $\sin\chi \sim 0$ shifts to lower frequencies, but the basic behavior of these functions remains the same.

As pointed out by Lichte [37,38], the role of the lens transfer properties on phase contrast imaging by defocus and by holography is thus clear. Defocus imaging of weak phase objects, as described by Eq. (5), depends on the $\sin\chi$ term. For a resolution of, say, 1 nm needed to achieve useful images of many elements of polymer morphology, the $\sin\chi$ term transfers almost no information from the exit-face wave phase to the image-wave amplitude. It is the latter that is recorded in a defocus experiment. A relatively small fraction of the actual phase shift is converted to amplitude information, and the contrast between the weak phase object and the background in this imaging mode is small. Holographic imaging of weak phase objects, on the other

hand, is described by Eq. (15) and is dominated by the cos χ term. In this case, the exit-face wave phase is almost entirely transferred through the lens to the image wave phase by a multiplicative factor of unity for a valuable range of spatial frequencies. Since holography recovers this phase directly, the contrast between the object and the background can be high despite the fact that the amplitude modulation is low.

5. Conclusions

Phase contrast TEM imaging offers an alternative to heavy-element staining approaches for studying morphology in nanoscale objects such as globular polymer particles. Using arborescent graft polystyrene nanoparticles, we have shown that holographic phase imaging can recover significant phase contrast from an object despite the fact that the amplitude contrast is negligible. Furthermore, knowing the mean inner potential of polystyrene, we have been able to recover a quantitative measure of the specimen thickness at all points in the specimen. In the present experiments, this ability enables us to conclude that the AGP particles on the carbon support film are not perfectly spherical but instead have a pancake shape. A comparison of the contrast generated by the holographic approach and that generated by the more traditional method of phase contrast transfer by defocus shows that there is significantly more contrast in the holographic phase image than in the defocused images.

Acknowledgements

This work was supported by the Army Research Office (grant #DAAG55-97-1-0137) and uses instrumentation jointly funded by the National Science Foundation and the New Jersey Commission on Science and Technology. The authors would like to thank Prof. Rob Briber (U. Maryland) for his early involvement in this work.

References

[1] Capek I. Adv Colloid Interf Sci 1999;80(2):85–149.
[2] Jikei M, Kakimoto M-A. Prog Polym Sci 2002;26(8):1233–85.
[3] Tomalia DA, Dvornic PR. Nature 1994;372(6507):617–8.
[4] Tomalia DA, Frechet JMJ, editors. Dendrimers and other dendritic polymers. Chichester: Wiley; 2001.
[5] Zeng F, Zimmerman SC. Chem Rev 1997;5:1681–712.
[6] Chou TM, Prayoonthong P, Aitouchen A, Libera M. Polymer 2002; 43(ER7):2085–8.
[7] Gajdardziska-Josifovska M, Carim AH. In: Voelkl E, Allard LF, Joy DC, editors. Introduction to electron holography. New York: Plenum; 1999. p. 267–93.
[8] O'Keeffe M, Spence JCH. Acta Crystallogr Sect A 1994;50:33–45.
[9] Rez D, Rez P, Grant I. Acta Crystallogr Sect A 1994;50:481–97.
[10] Saldin DK, Spence JCH. Ultramicroscopy 1994;55:397–406.
[11] Handlin DL, Thomas EL. Macromolecules 1983;16:1514–25.
[12] Handlin DL, Thomas EL. J Mater Sci Lett 1984;3(2):137–40.
[13] Roche EJ, Thomas EL. Polymer 1981;22(3):333–40.
[14] Blackson JH, Zhang X, Joy DC. In: Bailey GW, Garratt-Reed AJ, editors. Proceedings of the 52nd Annual Meeting of the Microscopy Society of America. New Orleans, LA: San Francisco Press; 1994. p. 126–7.
[15] Libera M, Gajdardziska-Josifovska M, Disko MM. In: Bailey GW, Garratt-Reed AJ, editors. Proceedings of the 52nd annual meeting of the Microscopy Society of America. New Orleans: San Francisco Press; 1994. p. 444–5.
[16] Libera M, Ott J, Wang YC. In: Tonomura A, editor. Electron holography. Amsterdam: Elsevier; 1995. p. 231–7.
[17] Simon P, Huhle R, Lehmann M, Lichte H, Monter D, Bieber T, Reschetilowski W, Adhikari R, Michler G. Chem Mater 2002;14: 1505–14.
[18] Simon P, Huhle R, Lichte H, editors. Proceedings of the 12th European Congress on Electron Microscopy EUREM 12, Brnó (Czech Republic); 2000. p. 327–8.
[19] Gabor D. Nature 1948;161(4098):777–8.
[20] Gabor D. Proc R Soc Lond A 1949;197:454.
[21] Tonomura A, Allard LF, Pozzi G, Joy DC, Ono TA. Electron holography. Amsterdam: Elsevier; 1995.
[22] Voelkl E, Allard LF, Joy DC. Introduction to electron holography. New York: Plenum; 1999.
[23] Wang YC, Chou TM, Libera M, Kelly TF. Appl Phys Lett 1997; 70(10):1296–8.
[24] Wang YC, Chou TM, Libera M, Voelkl E, Frost BG. Microsc Microanal 1998;4(2):146–57.
[25] Gauthier M, Moeller M. Macromolecules 1991;24(16):4548–53.
[26] Frank RS, Merkle G, Gauthier M. Macromolecules 1997;30(18): 5397–402.
[27] Gauthier M, Li W, Tichagwa L. Polymer 1997;38(26):6363–70.
[28] Striolo A, Prausnitz JM, Bertucco A, Kee RA, Gauthier M. Polymer 2001;42(6):2579–84.
[29] Cowley JM. In: Buseck P, Cowley J, Eyring L, editors. High-resolution transmission electron microscopy and associated techniques. New York: Oxford University Press; 1992. p. 38–57.
[30] Cowley JM, Spence JCH. In: Volkl E, Allard LF, Joy DC, editors. Introduction to electron holography. New York: Kluwer Academic/ Plenum Publishers; 1998. p. 17–56.
[31] Lichte H, editor. Advances in optical and electron microscopy, vol. 12. New York: Academic Press; 1991. p. 25–91.
[32] Tonomura A. Reviews of Modern Physics 1987;59(3):639–69.
[33] Choi S, Briber RM, Bauer BJ, Topp A, Gauthier M, Tichagwa L. Macromolecules 1999;32:7879–86.
[34] Sheiko SS, Gauthier M, Moeller M. Macromolecules 1997;30(8): 2343–9.
[35] Joy DC, Zhang YS, Zhang X, Hashimoto T, Bunn RD, Allard L, Nolan TA. Ultramicroscopy 1993;51:1–14.
[36] Mollenstedt G, Ducker H. Naturwissenschaften 1954;42:41.
[37] Lichte H. In: Bailey GW, editor. Proceedings of the 47th Annual Meeting of the Electron Microscopy Society of America. San Francisco: San Francisco Press; 1989. p. 2–3.
[38] Rau WD, Lichte H. In: Volkl E, Allard LF, editors. Introduction to electron holography. New York: Kluwer Academic/Plenum Publishers; 1998. p. 201–29.